Journal Title
XX(X):1–26

DOI: 10.1177/ToBeAssigned
www.sagepub.com/
SAGE

Experimental Investigation of the Fluctuating Static Pressure in a Subsonic Axisymmetric Jet

Songqi Li and Lawrence S. Ukeiley

Abstract

Measuring the fluctuating static pressure within a jet has the potential to depict in-flow sources of the jet noise. In this work, the fluctuating static pressure of a subsonic axisymmetric jet was experimentally investigated using a 1/8" microphone with an aerodynamically shaped nose cone. The power spectra of the fluctuating pressure are found to follow the -7/3 scaling law at the jet centerline with the decay rate varying as the probe approaches the acoustic near field. Profiles of skewness and kurtosis reveal strong intermittency inside the jet shear layer. By applying a continuous wavelet transform (CWT), time-localized footprints of the acoustic sources were detected from the pressure fluctuations. To decompose the fluctuating pressure into the hydrodynamic component and its acoustic counterpart, two techniques based on the CWT are adopted. In the first method the hydrodynamic pressure is isolated by maximizing the correlation with the synchronously measured turbulent velocity, while the second method originates from the Gaussian nature of the acoustic pressure where the separation threshold is determined empirically. Similar results are obtained from both separation techniques, and each pressure component dominates a certain frequency band compared to the global spectrum. Furthermore, cross-spectra between the fluctuating pressure and the turbulent velocity were calculated, and spectral peaks appearing around Strouhal number of 0.4 are indicative of the footprint of the convecting coherent structures inside the jet mixing layer.

Keywords

Jet noise, acoustic source, in-flow pressure measurements, wavelet analysis

University of Florida, Gainesville, USA

Corresponding author:
Songqi Li, Department of Mechanical and Aerospace Engineering, P.O. Box 116250, University of Florida, Gainesville, FL 32611
Email: songzi32@ufl.edu

Prepared using sagej.cls *[Version: 2017/01/17 v1.20]*

Introduction

Turbulence generated noise from subsonic jets represents fundamental flow phenomena that has a wide range of applications. The aviation community has made significant efforts at investigating jet noise since the advent of jet powered aircraft yet there are still many open questions as to the turbulent sources. From the commercial perspective, the noise level near airports has become an important factor limiting the growth of air traffic. During take-off, jet engines are responsible for most of the noise produced from the aircrafts, in which jet noise is the dominant noise source from the engine [1]. From the acoustic analogy work of Lighthill [2,3], a cause-effect relationship exists between the effect of turbulent flow and its induced far-field acoustics. Hence, examination of sound sources inside turbulent jets becomes a prerequisite for a detailed understanding of the mechanisms.

Acoustic sources in the jet mixing layer have been intensively investigated both numerically (for example, see Freund and Colonius [4] and Unnikrishnan and Gaitonde [5]) and experimentally. Non-intrusive measurements of fluctuating density, which is closely related to the pressure, have been performed by Panda and Seasholtz [6] to investigate the possible correlation with the far field acoustics. However, this Rayleigh-scattering-based approach will most likely fail when the jet is operated at low subsonic speeds [7] hence there is a need for direct measurements of the in-flow pressures. Direct measurements of the fluctuating static pressure in turbulent flows play an important role in identifying acoustic sources responsible for the sound generation. Various attempts have been made measuring the in-flow pressure fluctuations in subsonic, turbulent jets. Pioneering work can be traced back to the 1970s when Fuchs [8,9] first used circumferentially displaced standard condenser microphones with a streamline-shaped forebody to investigate the turbulence structures in a low speed jet. From the velocity-pressure correlations a wave-like pattern was captured which is consistent to the wavepacket model proposed by Mollo-Christensen [10]. The fluctuating static pressure was measured with a bleed-type pressure transducer by Jones *et al.* [11] to validate the spectral similarity laws at the low wavenumber range. George *et al.* [12] used a 1/8" condenser microphone sensor mounted in a Pitot-static tube to measure the in-flow pressure signals in a round jet, finding good agreements with the $k^{-11/3}$ and $k^{-7/3}$ laws which were derived from the pressure-Poisson equation. Despite the above-mentioned contributions, few studies have focused on detecting time-localized signatures of the acoustic sources from in-flow pressure measurements.

Wavepackets, defined as spatial and temporal modulated travelling waves, have been proposed to describe spatiotemporal structures in the jet and its radiated sound [13]. The footprint of wavepackets was first reported by Mollo-Christensen [10] and was described as semi-infinite line emitters for sound. Over the past years, wavepacket models have been intensively investigated experimentally and numerically. Wavepacket models indicate only a small portion of the energy from the acoustic sources will match linearized waves and propagate to the far field [14]. This problem was addressed by making a distinction between the acoustic pressure (sound) and the hydrodynamic pressure (pseudo-sound), with the acoustic component travelling to the far field and its hydrodynamic counterpart being convected downstream [15,16]. These distinctions highlight the necessity to separate the acoustic pressure from the hydrodynamic perturbations, from which one is able to isolate the portion of energy which is being radiated to the far-field and reduce the noise level by altering the flow structures through flow control techniques.

The possibility to separate hydrodynamic pressure from its acoustic counterpart originates from the phase speed associated with each component in the wavenumber–frequency space. A pressure component travelling subsonically and at the order of the flow velocity can be characterized as hydrodynamic, and the one with a phase speed greater than or equal to the speed of sound is classified as acoustic [17]. Several

attempts have been made to distinguish the acoustic sources measured in the jet near field, which is the region just outside the shear layer containing both acoustic and evanescent waves. Fourier-based filtering techniques has been reported by Tinney and Jordan[17] where the acoustic pressure was separated by its supersonic phase speed in the wavenumber-frequency domain. However, to resolve the appropriate wavenumber range a large number of microphones are required during the experiments. The intermittency of the convecting coherent structures and the induced acoustic near field[18–20] motivates the use of wavelet tools to capture localized events which are associated with the hydrodynamic pressure. Ukeiley and Ponton[21] first used wavelet analysis to investigate the streamwise evolution of the short-duration bursts measured from microphone arrays in the near field of a transonic jet. Furthermore, wavelet-based filtering techniques have been implemented to extract the intermittent component from the near field pressure and far field acoustic signals[22–24] .

In the present work, a subsonic axisymmetric jet was experimentally investigated in an attempt to identify sources in the hydrodynamic field. The fluctuating static pressure inside the jet shear layer was directly measured from a 1/8" microphone equipped with an aerodynamically-shaped nose cone and the evolution of the pressure spectra was analyzed. Two wavelet-based filtering techniques were applied in this work in an attempt to separate the acoustic pressure from the hydrodynamic perturbations. Additionally, cross-spectral analysis of the fluctuating pressure and the turbulent velocity were performed to explore the signature of the convecting coherent structures inside the jet mixing layer. The measurement and analysis techniques mentioned above provide insights characterizing acoustic sources and can be used to guide the development of noise suppression techniques.

Analysis Techniques

In this section a brief review of the analysis methods being used in this work are presented. The continuous wavelet transform will be introduced first, and the wavelet-based filtering techniques to separate the acoustic and hydrodynamic components are presented and discussed subsequently.

Continuous Wavelet Transform

The inherent intermittent nature of the fluctuating static pressure in turbulent jets facilitates the use of wavelet analysis which allows one to retrieve time-localized events from the original signals. The definition of the continuous wavelet transform (CWT) and some important properties will be briefly presented in the following. For a more detailed introduction one can refer to Mallat[25] and Torrence and Compo[26].

The CWT of a time sequence p' is defined as a convolution:

$$w(s,t) = \int_{-\infty}^{\infty} p'(\tau)\psi^*(\frac{t-\tau}{s})d\tau \tag{1}$$

where ψ represents the wavelet function and discussions of its properties can be found in Mallat[25]. The asterisk (*) indicates the complex conjugate. The dilatation factor, s, translates the wavelet function to different scales. This integral equation evaluates the similarity of the shape of the local signal and that of the transformed wavelet function. For a discrete time signal p'_n ($n = 0, 1, 2..., N-1$) with a sampling

period Δt, the CWT can be defined in an analogous manner as[26] :

$$W_n(s) = \sum_{m=0}^{N-1} p'_m \psi^* \left(\frac{(m-n)\Delta t}{s} \right) \tag{2}$$

in which m is the dummy index. In this manner one is able to depict how the amplitude of the convolution varies with scales and time. The complex-valued Morlet wavelet function ψ_0 is used in this work, which is mathematically formulated as:

$$\psi_0(\eta) = \pi^{-1/4} e^{i\omega_0 \eta} e^{-\eta^2/2} \tag{3}$$

Equation 3 describes travelling waves enveloped by a Gaussian window, in which ω_0 is a constant representing the angular velocity of the waves. In the following discussions $\omega_0 = 6$ is selected and the shape of the corresponding wavelet function is shown in Fig. 1. To make the wavelet coefficients $W_n(s)$ comparable to each other at each scale s, the wavelet function is normalized as,

$$\psi(n\Delta t/s) = \sqrt{\frac{2\pi s}{\Delta t}} \psi_0(n\Delta t/s) \tag{4}$$

In this work a total number of 300 scales s_j with fractional powers of two are chosen, such that $s_j = s_0 2^{j\delta_j}$ ($j = 0, 1, ..., J;\ J = 300$). s_0 is the smallest scale and δ_j determines the resolution. Furthermore, from the wavelet coefficients W_n, the original time sequence can be reconstructed by the following equation:

$$p'_{rec} = \frac{\sum_{j=0}^{J} \mathrm{Re}(W_n(s_j))/s_j^{1/2}}{\sum_{j=0}^{J} \mathrm{Re}(W_\delta(s_j))/s_j^{1/2}} \tag{5}$$

where $W_\delta(s) = \frac{1}{N} \sum_{k=0}^{N-1} \hat{\psi}^*(s\omega_k)$. $\hat{\psi}$ is the Fourier transformed wavelet function and ω_k represent the frequencies obtained from the discrete Fourier transform of p'_n.

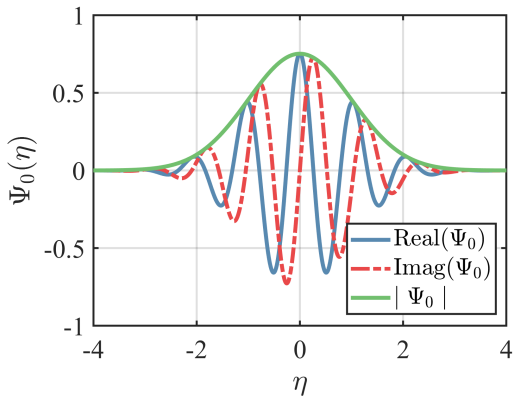

Figure 1. Shape of a Morlet wavelet with $\omega_0 = 6$.

CWT-based Hydrodynamic/Acoustic Pressure Separation Techniques

By definition, the hydrodynamic pressure represents the portion of the pressure possessing subsonic phase speeds in the wavenumber-frequency space, and it is quite unbiased by the compressibility in the flow[27]. Previous investigations on the near field pressure of subsonic jets[17,23] have shown that the hydrodynamic pressure is dominated by axially coherent structures at the low-frequency range. Meanwhile the acoustic counterpart is the pressure components owning supersonic phase speeds which is dominated by random fluctuations at higher frequencies. Similar behaviors should be expected for the in-flow pressure fluctuations. Because no wavenumber information can be obtained in the pressure signal measured from one microphone, in the present work the CWT is applied to separate the acoustic component from the pressure fluctuations p' measured inside the jet shear layer. The separation techniques are based on the assumption that the hydrodynamic component of the in-flow fluctuating pressure, which is associated with the convecting coherent eddies inside the flow field, correlates well with the compressed wavelet function[22], while the acoustic pressure associated with homogeneous and fine-scaled eddies are less significant in the time-scale space[23]. Therefore, by selecting a proper threshold T, the hydrodynamic component of the fluctuating pressure can be reconstructed using the wavelet coefficients exceeding the certain threshold in an absolute sense. This allows the wavelet coefficients to be divided into two portions, the part greater than T in magnitude is denoted by W_h, representing the hydrodynamic component of the signal p'_h, and the remaining coefficients which are less than the threshold is denoted by W_a, indicating the acoustic counterpart p'_a. It is obvious that selection of the threshold value T is crucial in the separation process. Two different methods that will be used in this work to determine the proper threshold, are introduced and discussed in the following.

Method 1. The first method requires synchronous measurements of the fluctuating pressure from the microphone and the single-point, streamwise turbulent velocity u', which in this work is measured from hotwire anemometry. Without loss of generality, the hotwire probe was fixed on the jet centerline and was in the same cross-stream plane as the pressure probe. The threshold T is optimized by maximizing the peak of $|\rho_{u'p'_h}(\tau)|$, which represents the absolute value of the cross-correlation coefficient between the hydrodynamic pressure and the fluctuating velocity. Fig. 2 shows the variation of $\max(|\rho_{u'p'_h}|)$ with different thresholds levels. At first the peak value increases gradually with T due to the reduction of the uncorrelated portion from the pressure. After reaching its maximum, the correlation peak decreases monotonically because the correlated portion of the original signal begins to be filtered out. In practice, a searching algorithm is implemented to locate both the maximum peak and the corresponding threshold value. The algorithm starts from an initial guess of the threshold denoted as T_0, then an iterative process with a varying threshold is executed until the optimized threshold with the maximized correlation peak is located.

Method 2. The second approach originates from the coherency extraction technique reported in Mancinelli *et al.*[23]. In this method only the in-flow pressure measurements are required, and the separation process is based on the random (Gaussian) nature of the acoustic pressure p'_a. Since the far field noise from subsonic jets has been shown to be Gaussian both experimentally and numerically[28,29], it is natural to postulate that the acoustic sources from the jet should possess the same property due to the causality relation between the acoustic sources and the radiated noise[30–33]. When modelling the acoustic pressure as an additive, Gaussian white noise, it has been demonstrated[29] that the ideal threshold

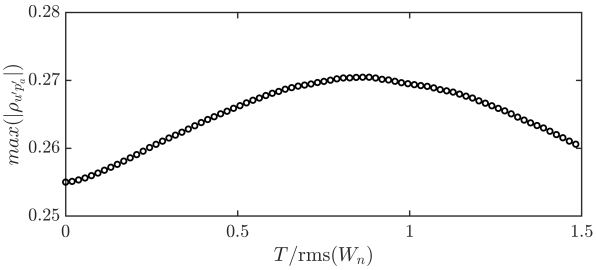

Figure 2. Variation of the absolute cross-correlation coefficient peak at different threshold levels. The threshold value is normalized by the variance of the wavelet coefficients. In this figure turbulent velocity was measured at $x/D = 5$, $r/D = 0$ and the fluctuating static pressure at $x/D = 5$, $r/D = 0.5$.

to remove the additive Gaussian white noise, in a min-max sense, is,

$$T = \sqrt{2\langle {p'_a}^2 \rangle \log_2 N_s} \tag{6}$$

where $\langle {p'_a}^2 \rangle$ is the variance of the acoustic pressure and N_s represents the total number of the sampling points. An iterative procedure is applied to seek the appropriate threshold value. Starting from the initial guess T_0:

$$T_0 = \sqrt{2\langle {p'}^2 \rangle \log_2 N_s} \tag{7}$$

The estimated threshold at each iteration is employed to extract the acoustic component from the original signal, which comprises wavelet coefficients less than the local threshold. Then the acoustic pressure is used to update the threshold estimation for the next iteration from Eqn. 6. The iterative process stops when the threshold converges to a certain value. As mentioned in Grizzi and Camussi[22], in this method the intermittent events are recognized based on their localized features in time and not of their shape, the results should be independent of the choice of the wavelet basis.

Experimental Setup

The experiments were carried out in the anechoic jet facility located in the Department of Mechanical and Aerospace Engineering at the University of Florida. A schematic of the facility can be found in Fig. 3. For more details of this facility refer to Mathew *et al.*[34] and Li *et al.*[35]. The axisymmetric subsonic jet nozzle is centered in front of the inlet of the wind tunnel, and has been installed to prevent unwanted recirculation occurring inside the chamber. The jet exit diameter is $D = 5.08$ cm with an area contraction ratio of 9:1. For Mach numbers $M = 0.3$ and 0.5, the corresponding Reynolds numbers are $Re_D = 3.8 \times 10^5$ and 6.4×10^5, respectively. A unitary Strouhal number $St = 1$ corresponds to a frequency of 2047 Hz.

A brief summary of the test conditions for different experiment campaigns is presented in Table 1. The fluctuating static pressure was measured using a Brüel and Kjær (B&K) Type 4138 1/8" microphone with a Type 2670 1/4" preamplifier as well as a suitable adaptor in between. The microphone has a dynamic range of 52.2 dB$\sim$168 dB (ref. 20 μPa) and a flat frequency response from 4 Hz to 100 kHz. To avoid

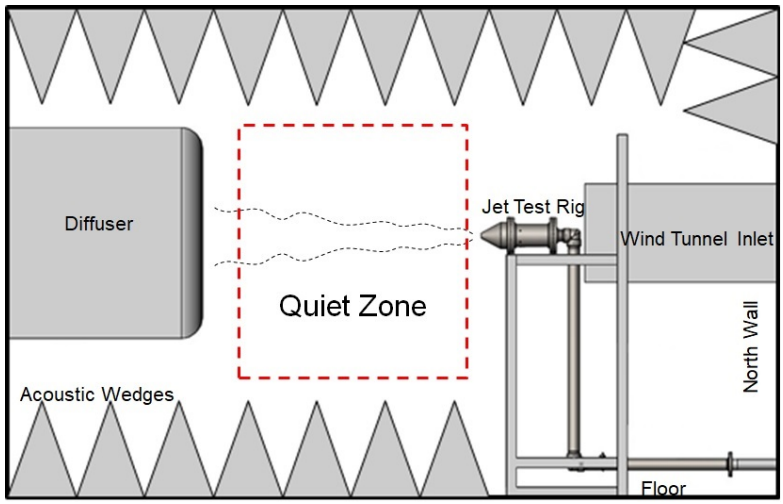

Figure 3. Schematic of the anechoic wind tunnel and the installation of the jet facility[35].

any contamination from total pressure fluctuations[36], an aerodynamically shaped nose-cone (B&K UA-0355) was installed on the microphone. The outer diameter of the nose-cone is 0.15", and the shape of the assembled probe is shown in Fig. 4. Taniguchi and Rasmussen[37] have shown the application of a nose-cone will significantly reduces the deviation in the microphone response equipped with a grid cap. Solderman and Allen[36] measured the microphone nose-cone free-field response at different frequencies, and found a small deviation around 2 dB at 10 kHz and 5 dB at 40 kHz. These results indicate that the installation of a nose-cone will generate negligible effect at the frequency range of interest (150∼20k Hz) in the current work. Although spatial filtering effects will exist when the microphone is placed in the flow, given the fact that the diameter of the nose-cone is only 1/13 of the jet diameter, the averaging effect will only emerge for fine-scale turbulence in the flow. Assuming fine-scale turbulence is locally isotropic[38] and the convection speed U_c is $\sim 0.7U_{CL}$ where U_{CL} represent the local centerline velocity, one may get a corresponding cut-off frequency St_c at the order of $\mathcal{O}(10)$ using $St_c = f_c\frac{D}{U_\infty} = \frac{U_c}{D_{mic}}\frac{D}{U_\infty}$. The microphone was mounted on a two-axis Velmex traverse system for precise motion along both the streamwise and the radial direction, and the positioning errors are less than 0.5 mm. The streamlined body of the microphone was aligned with the jet axis by a 1.5 mm thick laser sheet and the angular positioning error is less than 1°. The measurements focus on the regions where the turbulence generated noise originates, which is typically near the end of the potential core where the shear layer merges. As presented in Fig.5, at $x/D = 4, 5, 6$, the microphone was traversed throughout the jet shear layer from $r = 0D$ to $3D$ with 21 measurement points in between (here r refers to the distance with regard to the jet axis).

Far-field acoustic characterization was performed at $M = 0.5$ using a GRAS 46BE 1/4" free-field microphone fitted with a compatible preamplifier. The microphone has a dynamic range of 35 dB∼160 dB (ref. 20 μPa) and a flat frequency response up to 80 kHz. The microphone was mounted on a tripod boom microphone stand which was wrapped with sound absorbing materials to minimize acoustic reflection

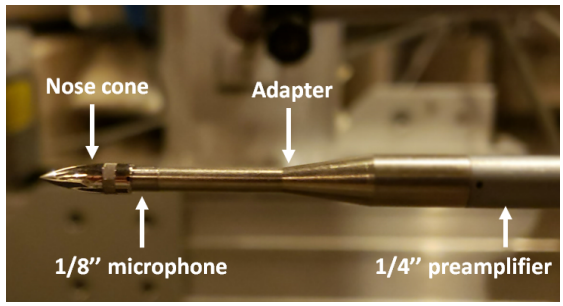

Figure 4. Configuration of the assembled pressure microphone with the B&K nose-cone in front.

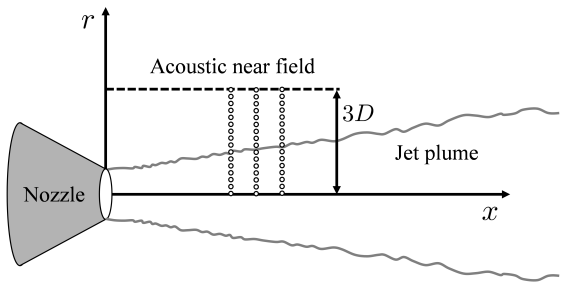

Figure 5. Schematic of microphone positioning for fluctuating static pressure measurements at $M = 0.3$.

from the stand. The microphone was adjusted to the same height as the jet axis and was orientated at normal incidence, pointing toward the center of the jet nozzle. The distances between the center of the jet exit and the microphone was fixed to $40D$ and the microphone was placed at different polar angles (ϕ) ranging from 40° to 110° with respect to the jet centerline ($\phi = 0$ is pointing downstream).

To extract the coherency of the pressure fluctuations with velocity, synchronous measurements of the turbulent streamwise velocity with the fluctuating static pressure were conducted. The velocity was measured from a Constant Temperature Anemometry (CTA) with a Dantec 55P11 miniature single hotwire probe. Two different experimental campaigns were carried out for synchronous measurements (see Fig.6). In the first set of experiments, the hotwire probe and the in-flow microphone were placed on the same cross-stream plane at $x/D = 5$. The hotwire was fixed on the jet axis by a non-adjustable strut and the microphone was radially traversed between $r = 0.2D$ and $1D$ with a uniform interval of $\Delta r = 0.1D$. The lower bound was chosen to avoid any interference between the probes, and the upper limit is where the microphone approaches the acoustic near field. To investigate the azimuthal dependence of the velocity-pressure correlation, the two probes were both placed at $x/D = 4$ and $r/D = 0.5$ in the second test campaign. Since the jet mixing layer is statistically axisymmetric in the azimuthal direction[39–42], the influence of the azimuthal angle between two probes was investigated by fixing the hotwire at a certain position while traversing the microphone azimuthally, such that the azimuthal angle between the two probes ($\Delta\theta$) ranges from 30° to 180°.

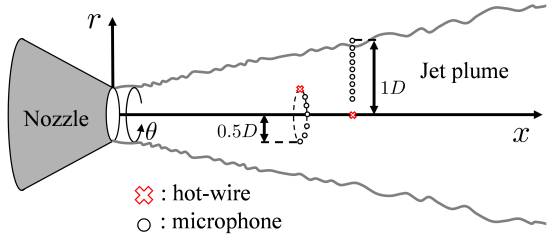

Figure 6. Two test campaigns for synchronous velocity-pressure measurements.

Table 1. A list of experiment campaigns and corresponding test conditions.

Experiments	Test conditions ($M = 0.3$ if not mentioned)
In-flow Pressure	$x/D = 4, 5, 6, r/D \leqslant 3$.
Far-field Acoustics	$R/D = 40$, $40° \leqslant \phi \leqslant 110°$, $M = 0.5$.
Synchronous #1	Velocity: $x/D = 5, r/D = 0$. Pressure: $x/D = 5, 0.2 \leqslant r/D \leqslant 1$.
Synchronous #2	Velocity: $x/D = 4, \theta = 0°$. Pressure: $x/D = 4, 30° \leqslant \theta \leqslant 180°$.

Data acquisition of single-point pressure, acoustic and velocity measurements was accomplished with a 24-bit NI PXI-4472 dynamic signal acquisition module. For all experiment campaigns listed in Table 1, a total number of 3.6×10^6 samples were acquired for each channel at each measurement point, and signals were sampled at 80 kHz and bandpass filtered between 150 Hz and 35 kHz. Major experimental uncertainty comes from the uncertainty of the jet exit Mach number ($\sim \pm 0.76\%$ of the target Mach number as reported in Li *et al.*[35]) and the positioning uncertainty of the microphone ($\pm 0.5mm$ in all directions, and $\pm 1°$ in angle).

Results and Discussions

Test Rig Validation

The mean streamwise velocity and the rms streamwise turbulent velocity field of the jet test rig at $M = 0.3$ was obtained from previous PIV measurements in Li *et al.*[35] and is presented in Fig. 7 for reference. The streamwise and the radial directions are denoted by x and r, respectively. The potential core is seen to collapse at $x/D = 5.73D$ where the shear layers merge and the centerline velocity becomes 95% of the nozzle exit velocity. Good agreement of the measured velocity profiles with previously published datasets[40,42] have been reported in Li *et al.*[35] which validate the jet properties in the current facility.

To characterize the directivity pattern of the far-field acoustics in the anechoic jet facility, the overall sound pressure level (OASPL) was exhibited in Fig. 8 as a function of the polar angle ϕ between $40°$

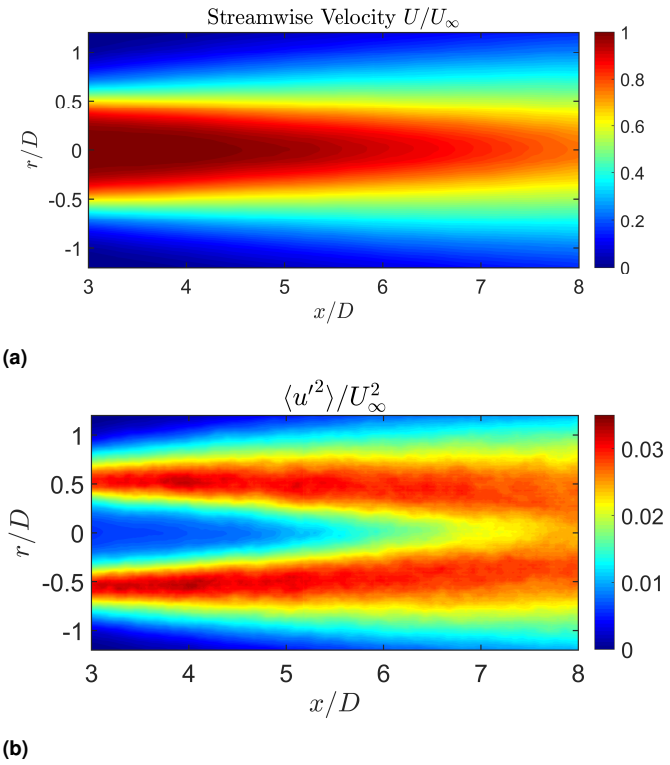

Figure 7. (a)Mean streamwise velocity and (b) rms turbulent streamwise velocity field from PIV at $M = 0.3$. Figures from Li *et al.*[35]

and $110°$. The sound level reaches its maximum at $40°$, then begins to attenuate as the polar angle keep increasing. The experimental results from Tanna[44] and LES results from Bodony[43] have also been plotted and were both scaled to a polar distance of $40D$ based on the method in Brown and Bridges[45]. Good consistency can be observed by comparing the sound levels measured from the current experiments with the existing data, which validates the quality of the acoustic measurements.

Figure 9 presents the power spectral density (PSD) of farfield acoustics measured at six different polar angles. The frequency has been non-dimensionalized to the Strouhal number which is defined as $St = fD/U_\infty$, and the amplitude of the spectra was divided by D/U_∞ according to Parseval's theorem before being converted into the logarithmic scale. The maximum sound levels appear at $\phi = 40°$, and the magnitude of the spectra decays as the polar angle increases. Additionally, Figure 10 exhibits the sound spectra at polar angles $40°$ and $90°$, along with the results reported in Cavalieri *et al.*[46] and Bridge and Brown[45], and satisfactory agreement can be observed from the comparison. In short, the anechoic jet facility used in this work is validated against different jet test rigs considering its flow and acoustic properties.

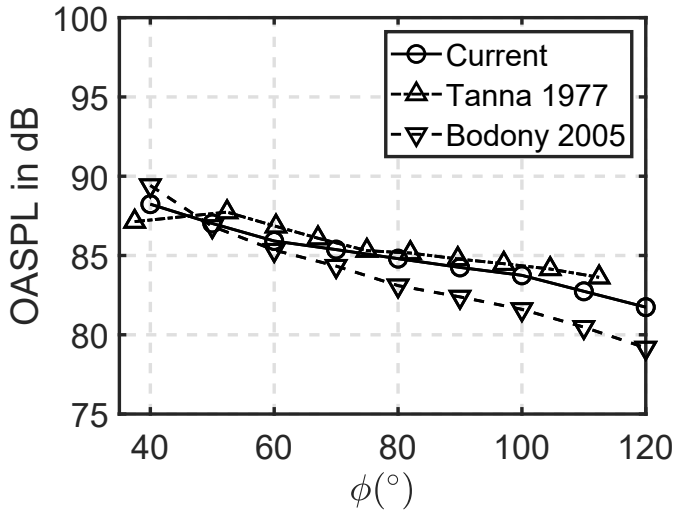

Figure 8. Comparison of OASPL (ref. $20\mu Pa$) at different polar angles from the current anechoic jet facility and Bodony[43] and Tanna[44] for $M = 0.5$. Data were scaled to a common distance of $40D$.

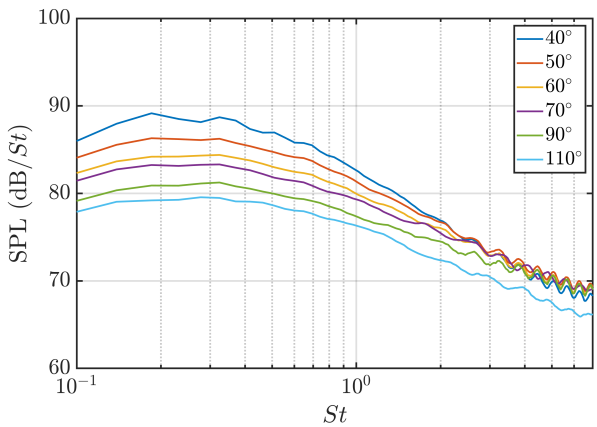

Figure 9. Power spectral density at different polar angles with a polar distance of $40D$.

In-flow Fluctuating Static Pressure Measurements

In order to capture the transition of the fluctuating static pressure before/after the potential core breaks down, the pressure was acquired at three different streamwise locations $x/D = 4, 5, 6$ which encompass the end of the potential core, and at each streamwise station the probe was radially traversed throughout the shear layer from the jet axis to the acoustic near field at $r/D = 3$. It should be noted that since both the hydrodynamic pressure and the acoustic pressure exist in the in-flow measurements, only a small

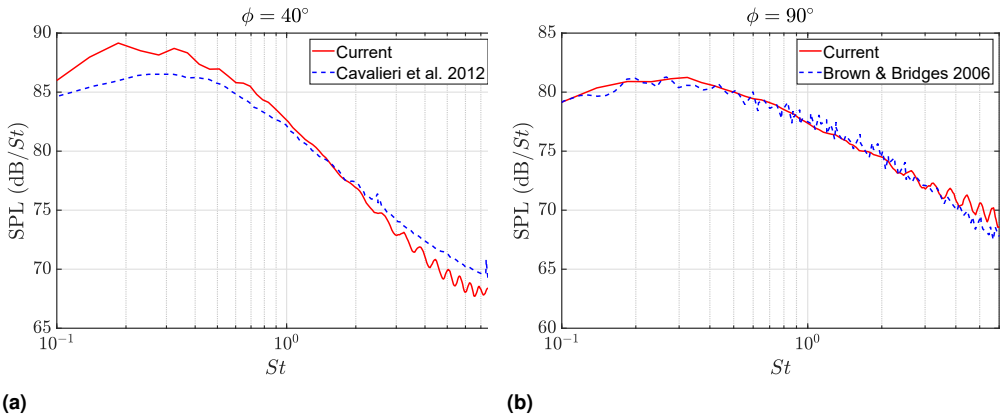

Figure 10. Comparison of PSD with the spectra from other test rigs at (a) $\phi = 40°$ and (b) $\phi = 90°$. Polar distances for all cases have been scaled to $40D$.

portion of the energy will propagate to the acoustic far field[13]. However, to evaluate the intensity of the pressure fluctuations inside the jet flow, the OASPL notation is still adopted in the following discussion by taking the logarithmic scale to the pressure fluctuations with regard to a reference value ($p_{ref} = 20\mu Pa$). Profiles of the OASPL measured at three different streamwise locations mentioned above are presented in Fig. 11. Along the radial direction, the OASPL peaks inside the jet shear layer (around $r/D = 0.5$), with a faster decaying rate on the ambient air side than on the jet axis side. As the pressure probe approaches the end of the potential core from $x/D = 4$ to 5, the fluctuating pressure remains the similar level inside the flow regime but holds a slower roll-off towards the ambient air side at $5D$ downstream, which leads to a 4.3 dB difference at $r/D = 3$. This is consistent with the finding reported in the literature (Bogey & Bailly[31], Tam *et al.*[47] among many other) that more energy is radiated out to the acoustic near field while approaching the end of the potential core. Since the potential core closes between $x/D = 5$ and 6, an attenuation of the OASPL at $6D$ downstream can be observed inside the jet mixing layer. However, such attenuation gradually disappears as the probe keeps moving radially, and the profiles measured at $5D$ and $6D$ downstream almost coincide with each other after $r/D = 1.75$. This phenomenon is consistent with the fact that the acoustic wavelength is larger than the nozzle diameter D.

The skewness of the static pressure fluctuations is presented in Figure 12 as a function of the radial location, which sheds light on the asymmetry of the probability distribution functions. In jet flows negative skewness factors have been shown to likely be linked with the appearance of vortical structures[48]. For all three streamwise stations, a negative peak can be detected between $r/D = 1$ and 1.5. From $4D$ to $6D$ downstream, the negative peak becomes more pronounced and the radial location of the peak gradually moves outward. Comparing peak locations to the rms streamwise turbulent velocity profiles in Figure 7b, one may find the peaks residing on the outer edge of the expanding jet shear layer where the vortical structures are generated by the entrainment effect. The increased magnitude of the absolute skewness along the streamwise direction may suggest the vortical structures become more and more prevalent as the flow travels downstream. When $r/D > 2$, the skewness factor approaches zero, indicating intensive events can rarely be detected in the jet near field. Furthermore, because of the decay

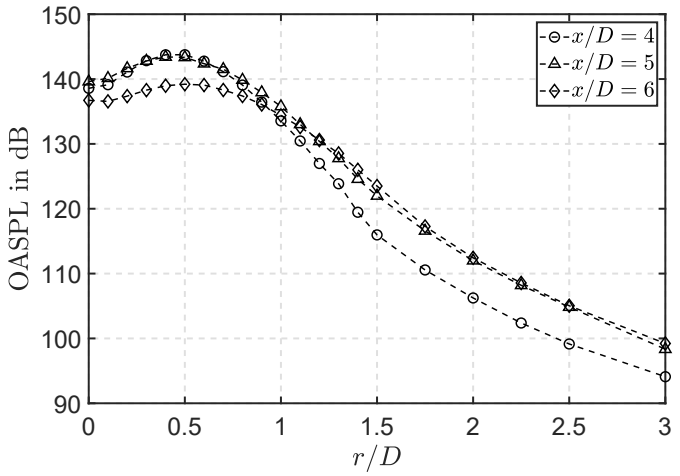

Figure 11. OASPL measured at $x/D = 4, 5, 6$ with radial locations between $0D$ and $3D$.

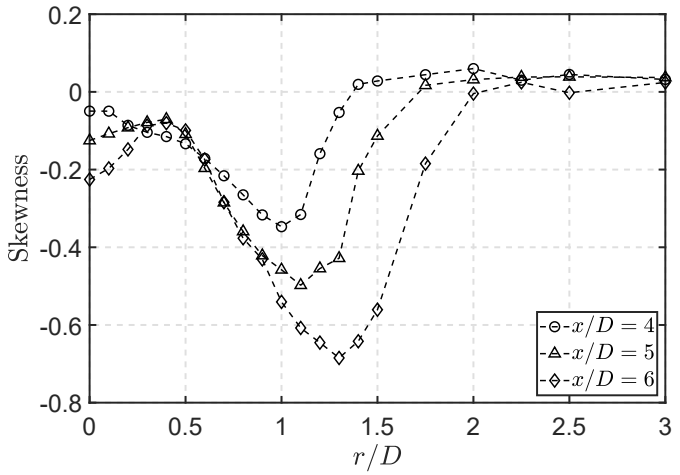

Figure 12. Skewness of the fluctuating pressure measured at $x/D = 4, 5, 6$.

of the jet core, the absolute value of the skewness factor at the jet centerline is found to increase along the streamwise direction, which coincides with the fact that the flow on the jet axis becomes turbulent after the potential core closes.

To evaluate the intermittent events from the signal, the kurtosis of the fluctuating static pressure is plotted in Figure 13 with varying r. Similar to the previous discussions, a peak formed at the outer edge of the jet shear layer can be observed in all three cases. After careful examination, one may find the peak locations in Figure 13 are close to the ones in Figure 12. Comprehensively, these facts imply the appearance of intermittent structures around the peak locations which hold large vorticity will induce

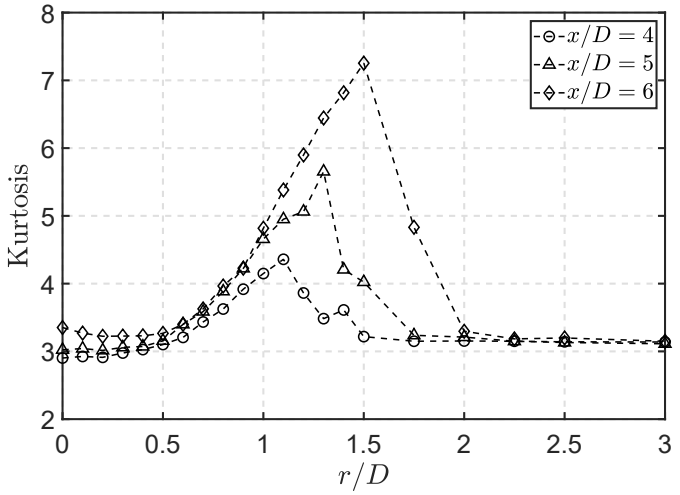

Figure 13. Kurtosis of the fluctuating pressure measured at $x/D = 4, 5, 6$.

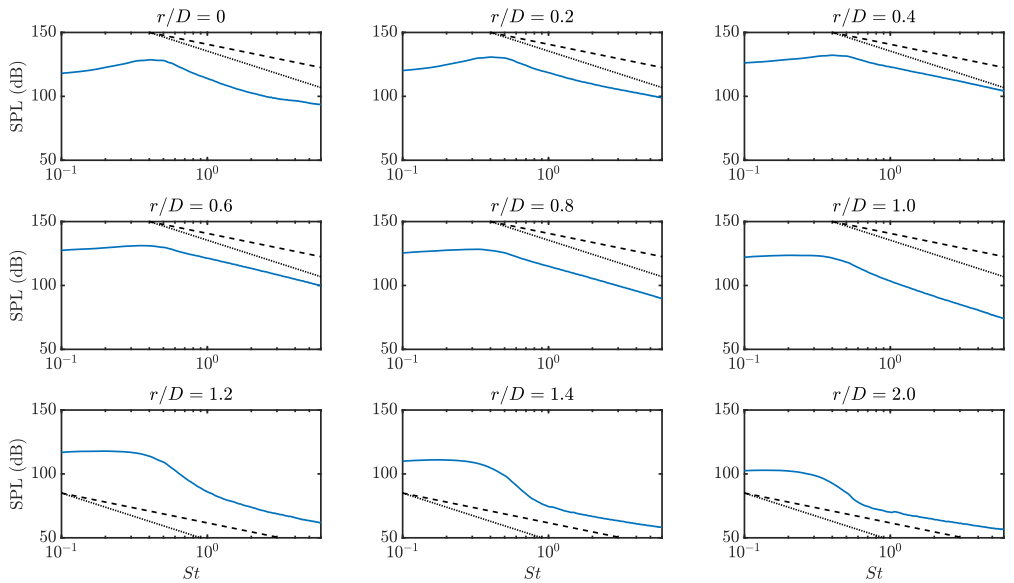

Figure 14. Pressure spectra at different radial locations for $x/D = 4$. Dashed line (- - -): $-7/3$ line; dotted line (·····): $-11/3$ line.

negative pressure fluctuations. After reaching the peak, a rapid attenuation occurs and the Kurtosis factor tends to approach 3 , indicating the Gaussian nature of the pressure fluctuations[49] as the probe approaches the acoustic near field.

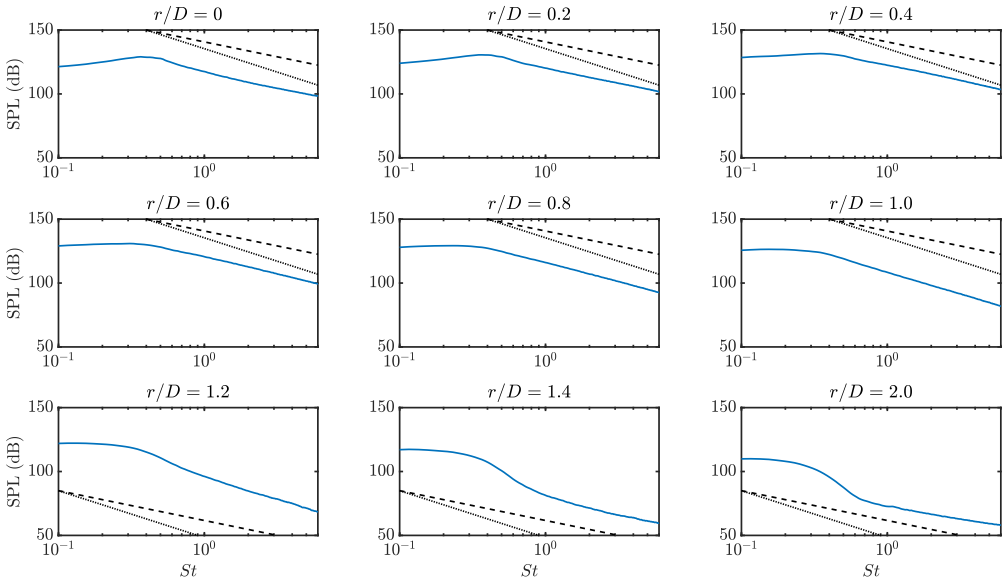

Figure 15. Pressure spectra at different radial locations for $x/D = 5$. Dashed line (- - -): $-7/3$ line; dotted line (·····): $-11/3$ line.

Figures 14 to 16 show the sound pressure levels calculated at 9 different radial locations ranging from the jet axis to the entrainment region for $x/D = 4, 5, 6$, respectively. The classic $-7/3$ and $-11/3$ scaling laws from George *et al.*[12] are also plotted for comparison, in which the slope of $-7/3$ represents the effect of the second order turbulence-shear interactions and the $-11/3$ law is a result of the turbulence-turbulence interactions. Although some spurious spikes occasionally appear in the power spectra (for example, the one at $St \approx 3$ for $r/D = 1$ in Figure 14), these spikes are essentially electrical noise and won't affect the overall trend of the spectral rolling-of rate. For $x/D = 4$ (see Figure 14), the spectra peaks around $St = 0.4$ when $r/D \leqslant 0.4$, followed by an power-law roll-off asymptotic to $-7/3$ at the high frequency range. At $r/D = 0$, this rapid decay slows down when the Strouhal number is greater than 2, which is due to the initial turbulent fluctuations generated inside the piping and the jet plenum. From $r/D = 0.6$ to 1, the Strouhal 0.4 peak is replaced by a broadband event between $St = 0.1$ and 0.3. At the same time, the roll-off rate at high frequencies steadily increases and asymptotes to $-11/3$ at $r/D = 1$. Moving outward, the pressure probe approaches the acoustic near field and the pressure spectra begin to possess the characteristics of the near field spectra, with a fast decay rate inside the inertial subrange followed by a slower roll-off in the range of the propagating pressure field as defined in Arndt *et al.*[50].

At $x/D = 5$ (Figure 15), the pressure probe is closer to the end of the jet core in the streamwise direction. Similar to the observations at $4D$ downstream, pressure spectra measured near the jet centerline peak around $St = 0.4$, then ~~exponentially~~ decay with a $-7/3$ roll-off at high frequencies. In this case the spectrum measured at $r/D = 0$ keeps decaying with the constant slope for large Strouhal numbers since the sound level at the high frequency range overwhelms the initial fluctuations mentioned above. As the radial distance r continues increasing, the spectral decay rate continuously raises and a $-11/3$ law

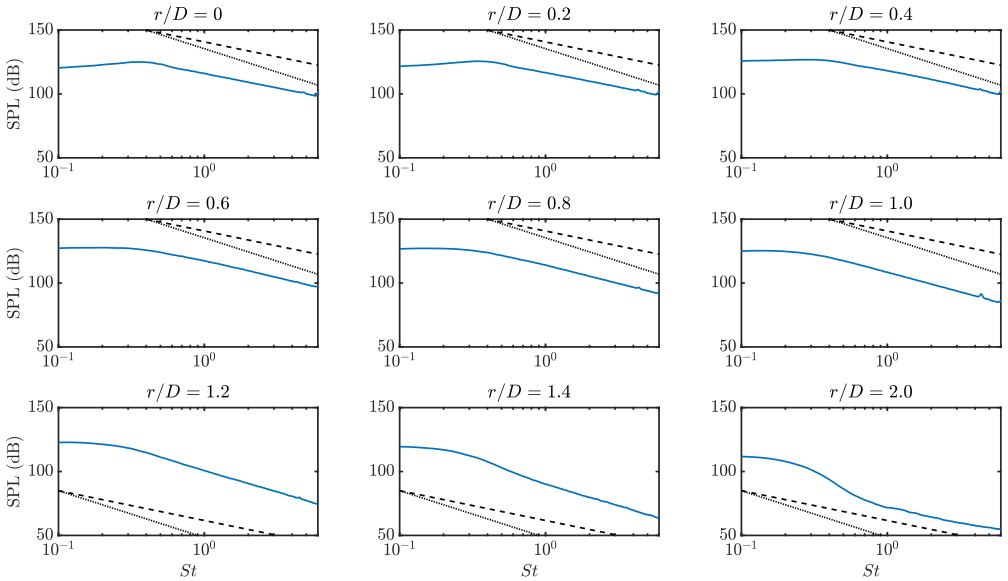

Figure 16. Pressure spectra at different radial locations for $x/D = 6$. Dashed line (- - -): $-7/3$ line; dotted line (·····): $-11/3$ line.

is achieved around $r/D = 1$, meanwhile the Strouhal number 0.4 peak gradually disappears from the spectra. From then on, the probe moves towards the acoustic near field, and the inertial subrange as well as the region of the propagative pressure field can be clearly seen from the pressure spectra at $r = 2D$. Identical trends can be observed for $x/D = 6$ (Figure 16), including the transition from the $-7/3$ law to the $-11/3$ law, the disappearance of the $St = 0.4$ peak, and the evolution to the near field features as r keeps increasing. The only differences are the overall magnitude of the individual spectrum which will account for the OASPL profiles shown in Figure 11, and the radial transition intervals which is caused by the radial expansion of the jet shear layer when the flow moves downstream.

The pressure spectra measured from $r/D = 3$ have been compared with the near field acoustic data by Ponton *et al.*[51] at three streamwise locations, which are shown in Figure 17. Based on the power laws introduced in Arndt *et al.*[50], the $-20/3$ and -2 lines are also plotted which represents the scaling laws at the inertial subrange and the propagative pressure field, respectively. The near field pressure spectra from Ponton *et al.*[51] were acquired from a linear microphone array and the microphones were orientated perpendicular to the jet axis while in the current measurements the pressure probe was placed parallel to the axial direction. In spite of the distinct experimental setup, the two sets of pressure spectra coincide well with each other. Furthermore, a power-law decay with a slope of $-20/3$ followed by a -2 roll-off exists in all three cases which is consistent with the theoretical scaling laws.

Synchronous Measurements

The experimental results from synchronous pressure-velocity measurements will be discussed in this subsection. One general concern for synchronous in-flow measurements with two or more probes comes

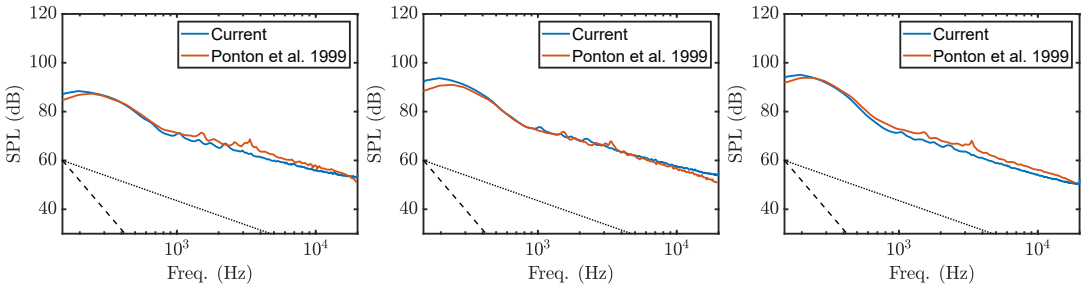

Figure 17. Pressure spectra measured at $r/D = 3$ for (a) $x/D = 4$, (b) $x/D = 5$, and (c) $x/D = 6$ and comparison with Ponton *et al.*[51]. Dashed line (- - -): $-20/3$ line; dotted line (·····): -2 line.

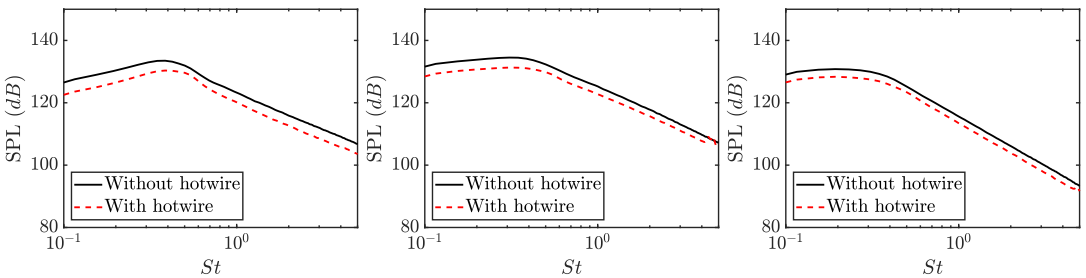

Figure 18. Effect of the the hotwire probe at $r/D = 0$ to the pressure spectra at (a) $r/D = 0.2$, (b) $r/D = 0.5$, (c) $r/D = 0.9$. Both probes are at $x/D = 5$.

from the possible interaction among probes. Therefore, as a precursor to further signal processing procedures, the effect of noise generated by the hotwire probe on the in-flow pressure measurements was first examined. Figure 18 presents the pressure spectra measured individually at $r/D = 0.2, 0.5, 0.9$ for $x/D = 5$, as well as the pressure spectra measured at the same locations with the hotwire probe in the flow at $r/D = 0$, $x/D = 5$. Although a slight attenuation (around 3 dB) of the spectral amplitude may be seen from the synchronously measured pressure spectra, little difference has been found with respect to the spectral shape throughout the jet shear layer. These observations indicate there is negligible effects of noise generated by the hotwire probe being introduced to the in-flow pressure measurements.

The time-lagged velocity-pressure correlation coefficients ($\rho_{u'p'}(\tau)$) at $x/D = 5$ are presented in Figure 19. The pressure was measured at nine equally-spaced radial locations r with $\Delta r/D = 0.1$, and the velocity was measured on the jet centerline in all cases. The time lag, τ, is scaled by the nozzle outlet diameter D and the jet exit speed U_∞. The contours of $\rho_{u'p'}$ in Figure 19b are plotted by vertically stacking the cross-correlation results obtained at all r's. In all instances, significant wavepacket envelopes can be clearly observed, each possessing one negative peak and two positive but asymmetric side lobes. This indicates the pressure fluctuations are always in anti-phase with the centerline streamwise

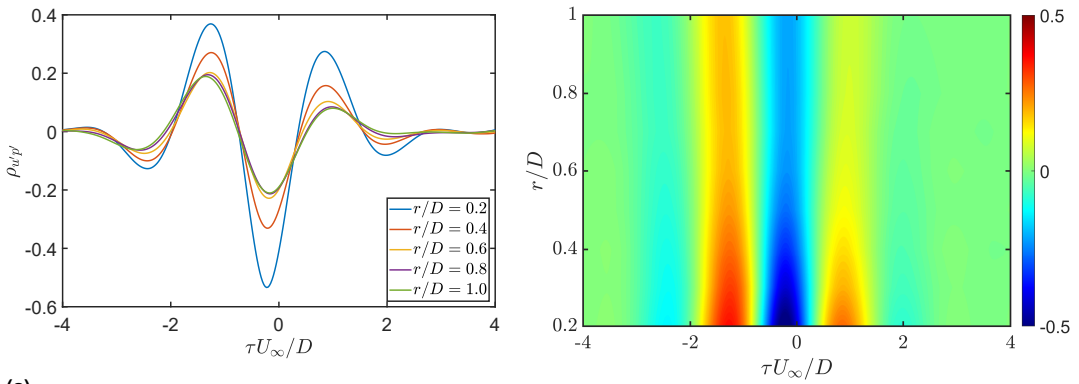

Figure 19. Time-lagged cross-correlation coefficients $\rho_{u'p'}$ with different radial separations at $x/D = 5$. Velocity was measured at $r/D = 0$ and pressure at different radial locations between $0.2D$ to $1D$. (a) $\rho_{u'p'}$ at five representative radial locations r; (b) the contour of $\rho_{u'p'}$.

velocity throughout the jet shear layer, which is consistent with the discussion of the phase relationship between pressure fluctuations and streamwise velocity in the jet core by Lau *et al.*[52]. The strongest correlation appears at $r/D = 0.2$ when the two probes are closest to each other and $\rho_{u'p'} \approx 0.53$ at the negative peak. As r increases, the overall magnitude of the wavepacket envelope is attenuated, and a rapid loss of correlation occurs before $r/D = 0.6$. Since the hydrodynamic component of the fluctuating pressure is highly correlated to the coherent structures passing by the jet mixing layer, the fast decay of coherency should be a result of the exponential decay of the hydrodynamic pressure fluctuations along the radial direction. Although the coherency decay is still recognizable after $r/D = 0.6$, the damping effect becomes weaker, and the magnitude of the negative peak maintains a level around -0.18 when $0.6 \leqslant r/D \leqslant 1$. According to Cavalieri *et al.*[53] and Batchelor & Gill[54], only axisymmetric streamwise velocity component will exist on the jet axis. Therefore, these radially separated cross-correlation results will serve as a reference to evaluate the intensity of axisymmetric coherent structures in the radial direction.

As a measure of the correlation level between two signals, the cross-spectra obtained at $r/D = 0.3, 0.6, 0.9$ are examined in Figure 20. Similar to the autospectra of p' presented above, a peak around Strouhal number 0.4 can be clearly captured in all 3 cases, which represents the footprint of large-scale structures being convected downstream. Additionally, the magnitude of the cross-spectra peaks reduces with increasing r, which indicates a loss of coherence as the pressure probe moves outward. At higher frequencies, the cross-spectra are submerged into the instrumentation uncertainty which limits the resolvable bandwidth for Strouhal number greater than 0.8.

Similarly, the azimuthal dependence of the velocity-pressure correlation coefficients is investigated and shown in Figure 21, with both u' and p' measured at $x/D = 4$ and $r/D = 0.5$. The upper bound of the azimuthal separation angle $\Delta\theta$ is set to $180°$ due to the symmetry in the cross-stream plane, and the lower bound $\Delta\theta = 30°$ was chosen to avoid possible interference between probes and from support

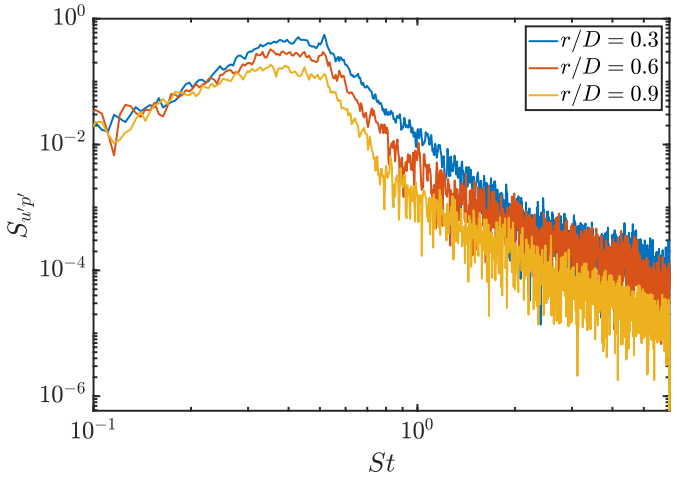

Figure 20. Velocity-pressure cross-spectra measured at $r/D = 0.3, 0.6, 0.9$ for $x/D = 5$.

struts. Figure 21b was generated using the same method in Figure 19b, and the azimuthal resolution is 30° in this case. For each discrete $\Delta\theta$ value, the locations of the four most significant peaks/troughs have been marked by black dots, and the dots were grouped into five polylines 1 to 5 to represent the azimuthal evolution of the wavepackets. In general, the overall correlation level drops down significantly compared to the results in Figure 19, and the maximum correlation level in Figure 21b is merely around 0.08. This indicates the flow structures that govern the jet lipline are less coherent than the ones passing through the jet centerline. At $\Delta\theta = 30^\circ$, as shown in Figure 21b, the dominant feature of the cross-correlation coefficients can be described as a $(+ - +-)$ wavepacket (from left to right), which contains a pair of opposite-signed peaks possessing similar magnitudes and two opposite-signed side lobes which are weaker than the main peaks. The main peaks can be represented by lines (3, 4) and the side lobes by lines (2, 5). Similar descriptions also apply to $\Delta\theta = 45^\circ$ (in Figure 21a) and 60° cases. The $(+ - +-)$ pattern is sill distinguishable at $\Delta\theta = 90^\circ$ (see lines 2, 3, 4, 5), however, in this case the magnitudes of main peaks have been attenuated to the same level as the side lobes. The interval $90^\circ \leqslant \Delta\theta \leqslant 120^\circ$ can be best described as an intermediate stage. In this stage, a new side lobe 1 emerges from the left, and the original side lobe 2 is gradually intensified and becomes a new main peak. The amplitude of peak 3 is gradually recovered and groups with peak 2 to form a new pair of opposite-signed main peaks. Nevertheless, the original main peak 4 is weakened and eventually becomes the new side lobe on the right, at the same time the original side lobe 5 is flattened and becomes unrecognizable after 120°. Following the above-motioned process, the wavepacket is transformed into a $(- + -+)$ structure with two main peaks (2, 3) and side lobes (1, 4). After this peak-relocating process, the amplitude of the wavepacket continues to raise and the overall magnitude at 180° becomes comparable to the one at 30°. Besides the shape transformation of the wavepacket, the wavepacket also travels in time as the distance between the two probes keeps increasing, and the travelling speed, which can be represented by slopes of the lines, is directly related to the change of the linear distance between the probes when the microphone moves from one azimuthal angle to another. These comprehensive effects result in a nearly 180° phase change

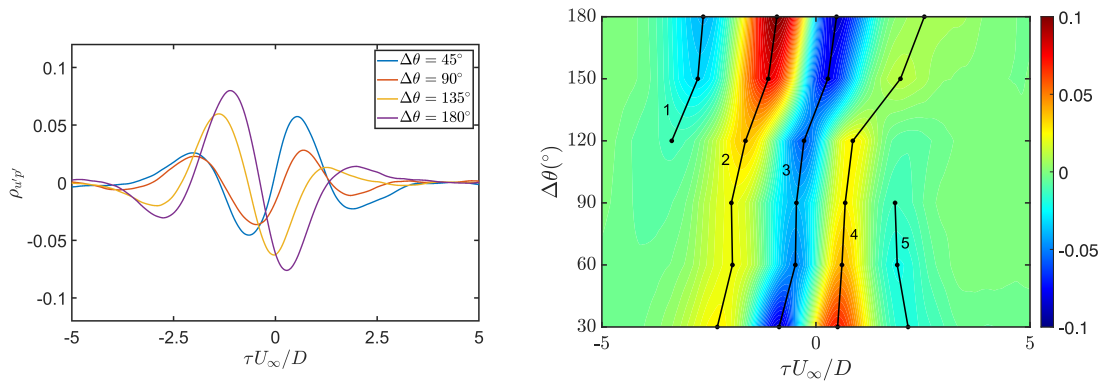

Figure 21. Time-lagged cross-correlation coefficients $\rho_{u'p'}$ with different azimuthal separations at $x/D = 4$ and $r/D = 0.5$. (a) $\rho_{u'p'}$ at five representative azimuthal separation angles $\Delta\theta$; (b) the contour of $\rho_{u'p'}$ in which black dots $(\cdot)$ represents the locations of the four most significant peaks in $\rho_{u'p'}$ at six different $\Delta\theta$'s.

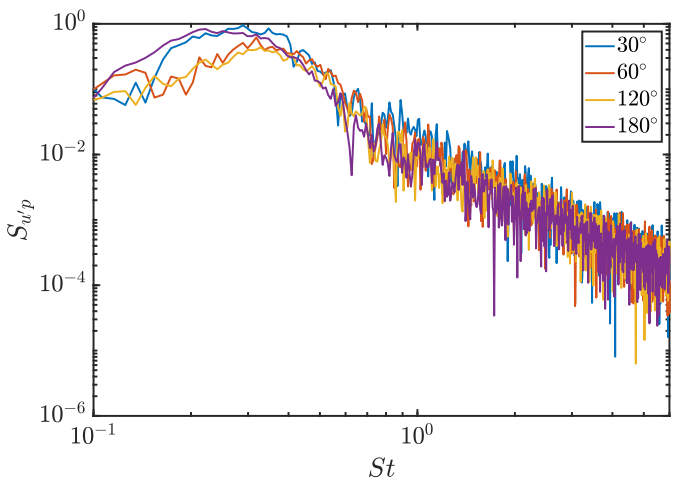

Figure 22. Velocity-pressure cross-spectra with different azimuthal separations ($\Delta\theta = 30°, 60°, 120°, 180°$). Both u' and p' were measured at $x/D = 4$ and $r/D = 0.5$.

of the wavepacket shape from $\Delta\theta = 30°$ to $180°$, which exhibits significant similarity to the behavior of a helical mode in azimuth.

Figure 22 presents the cross-spectra obtained at 4 different azimuthal separation angles with $x/D = 4$ and $r/D = 0.5$ for both velocity and pressure measurements. For all test cases, the spectra are found to peak between Strouhal number 0.2 and 0.4, indicating the strong coherency of u' and p' in the low frequency range around the azimuthal direction. In higher frequencies, as the result of random phased,

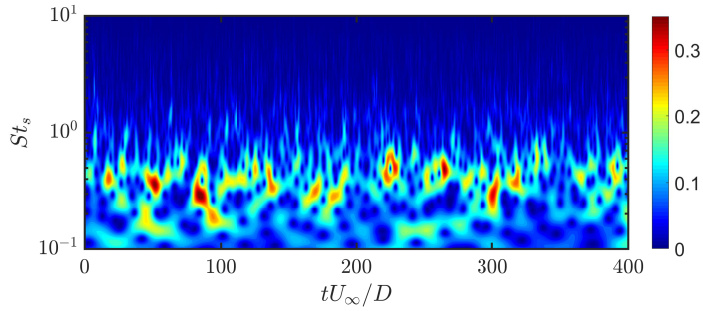

(a) $r/D = 0.3$.

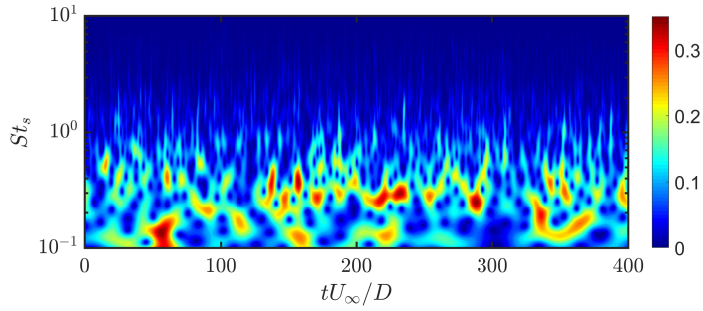

(b) $r/D = 0.6$.

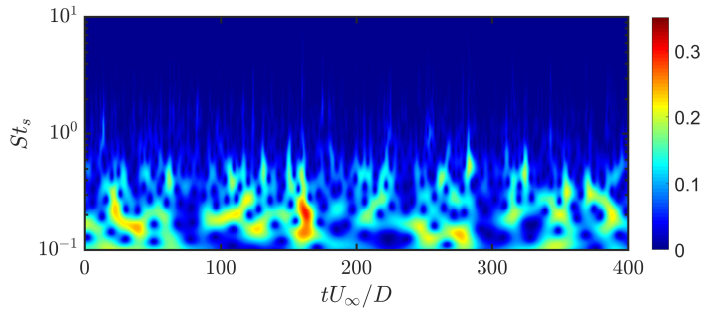

(c) $r/D = 0.9$.

Figure 23. Non-dimensionalized wavelet scalograms $|w|$ at x/D=5 over a short time period.

smaller-scaled vortices inside the flow, a power-law decay of the cross-spectra is still recognizable, this trend is overwhelmed by the extraneous instrumentation noise from both measurement results.

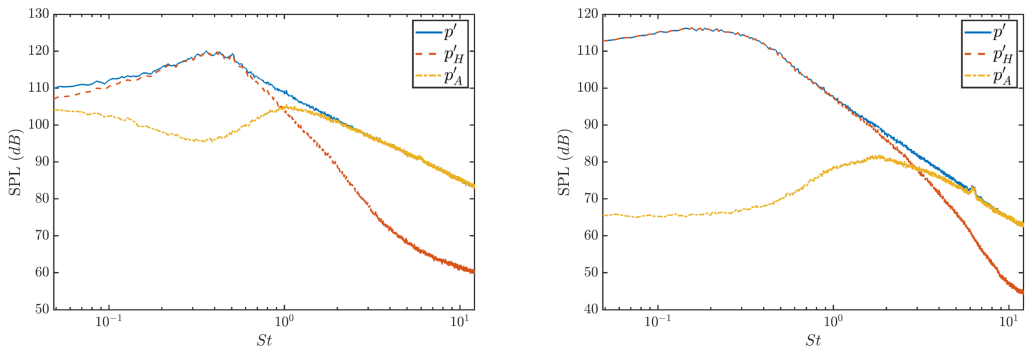

Figure 24. SPLs of the original, hydrodynamic and acoustic pressure (named p', p'_H, p'_A, respectively) measured at $x/D = 5$ using Method 1. (a) $r/D = 0.2$ and (b) $r/D = 1$.

Wavelet Analysis and Acoustic/Hydrodynamic Pressure Separation

One disadvantage of Fourier-based analysis techniques is the lack of ability to capture events with short durations and localize them in time. On the contrary, wavelet analysis is able to provide this missing piece of information by convolving the time series with the wavelet basis function at different scales. Figure 23 shows the pressure scalogram over a short time period at $r/D = 0.3, 0.6, 0.9$ for $x/D = 5$, in which the time is non-dimensionalized as tU_∞/D and the wavelet coefficients are scaled by the dynamic pressure $\frac{1}{2}\rho U_\infty^2$, such that the scalogram levels are comparable. The temporal scale s is transformed into the pseudo-frequency[26] f_s and is converted to the pseudo-Strouhal number defined as $St_s = f_s D/U_\infty$. The red areas of the scalograms highlight the intense, time-localized activities from the pressure signal, which identify the signature of the intermittent sources in the flow. At $r/D = 0.3$ which is close to the jet centerline, intense source activities can be detected, which are compact in time and are mostly concentrated inside a frequency band centered at $St_s = 0.4$. At $r/D = 0.6$, more source activities are highlighted from the scalogram, most of which possess a similar order of magnitude but are less compact compared to the previous case. Meanwhile, more low frequency content appears around $St \approx 0.1$, and the dominant frequency band becomes a more broadband one which extends between $0.1 \leqslant St_s \leqslant 0.5$. As the pressure probe continues traversing away from the acoustic sources, at $r/D = 0.9$, the source activities become more dispersed in its temporal and frequency extensions, and apparent attenuation is found from the overall level of the wavelet coefficients. The dominant frequency band in this case is within $0.1 \leqslant St_s \leqslant 0.4$, which is consistent with the properties of the pressure spectrum in Figure 15 at $r/D = 1$.

To separate the hydrodynamic pressure from its acoustic counterpart, the two different methods which have been introduced above were applied to the pressure measured at $x/D = 5$, and results will be discussed below. Figure 24 shows the SPL spectra of the original pressure signal as well as the hydrodynamic and acoustic components at $r = 0.2D$ and $1D$ from Method 1, in which synchronous sampling of turbulent velocity and pressure fluctuations was involved. In this method, the hydrodynamic pressure is the portion of the pressure fluctuations that correlates well with the velocity measured at the jet

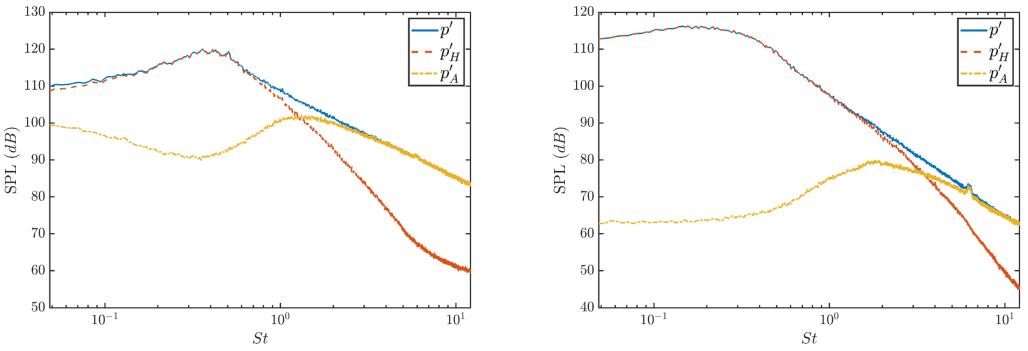

(a) $r/D = 0.2$. **(b)** $r/D = 1$.

Figure 25. SPLs of the original, hydrodynamic and acoustic pressure (named p', p'_H, p'_A, respectively) measured at $x/D = 5$ using Method 2. (a) $r/D = 0.2$ and (b) $r/D = 1$.

centerline and the acoustic pressure represents the residue. For both radial locations, the hydrodynamic component preserves the properties of the original pressure spectra at low-middle frequencies, especially around the low frequency peaks which are associated with the large-scale coherent structures inside the jet mixing layer. Then the hydrodynamic pressure decays rapidly and becomes insignificant at high frequencies. The acoustic pressure, on the other hand, follows the original spectra faithfully in the higher frequency range. Comparatively it holds a broadband energy distribution although the energy contained at low frequencies is still trivial compared to the original signal for both instances.

Similar features can be found from the separation results implemented by Method 2, in which the threshold was determined empirically from Equation (6). As displayed in Figure 25, the hydrodynamic pressure dominates the region at low-middle frequencies including the low frequency peak, while the acoustic counterpart matches the global spectra at the high frequency range. Although for both instances ($r/D = 0.2$ and 1) the acoustic pressure contains lower energy levels comparing to results from Method 1, no significant difference between the two methods was noticed with regard to the major characteristics of the hydrodynamic/acoustic spectra.

Conclusions

In the present work a subsonic axisymmetric jet was examined experimentally. Direct measurements of the fluctuating static pressure describe the transition of the OASPL and the power spectra from the jet centerline to the acoustic near field at $x/D = 4, 5, 6$, and different scaling laws are observed at different stages as the pressure probe moves radially. Cross-correlation and cross-spectra between pressure and velocity with radial and azimuthal separations both indicates strong coherency around $St = 0.4$. Furthermore, profiles of skewness and kurtosis coefficients indicate strong intermittent events inside the flow region, and a continuous wavelet transform was employed to extract the time-localized bursts from the pressure signals.

In an attempt to separate the hydrodynamic fluctuations from the acoustic pressure, two wavelet-based separation techniques were adopted. They are based on the coherency between turbulent velocity and hydrodynamic pressure and the Gaussian nature of the acoustic pressure, respectively. Good agreement can be found from the individual spectra and in general the hydrodynamic component dominates the low-middle frequency band while the acoustic counterpart governs a higher frequency band. These observations can be used to shed light on how to improve the noise mitigation of subsonic jets through various flow control techniques. Specifically, by introducing excitation to alter the flow field events associated with the generation acoustic pressure signature.

Acknowledgements

The authors acknowledge the support of the National Science Foundation (NSF) under award CBET-1704768.

References

1. Zaporozhets O, Tokarev V and Attenborough K. Aircraft Noise: Assessment, prediction and control. CRC Press, 2011.
2. Lighthill MJ and Newman MHA. On sound generated aerodynamically I. general theory. Proceedings of the Royal Society of London Series A Mathematical and Physical Sciences 1952; 211(1107): 564–587. DOI: 10.1098/rspa.1952.0060.
3. Lighthill MJ. On sound generated aerodynamically II. turbulence as a source of sound. Proceedings of the Royal Society of London Series A Mathematical and Physical Sciences 1954; 222(1148): 1–32. DOI: 10.1098/rspa.1954.0049.
4. Freund JB and Colonius T. Turbulence and sound-field POD analysis of a turbulent jet. International Journal of Aeroacoustics 2009; 8(4): 337–354. DOI:10.1260/147547209787548903.
5. Unnikrishnan S and Gaitonde DV. A pressure decomposition framework for aeroacoustic analysis of turbulent jets. European Journal of Mechanics - B/Fluids 2020; 81: 41–61. DOI:10.1016/j.euromechflu.2020.01.006.
6. Panda J and Seasholtz RG. Experimental investigation of density fluctuations in high-speed jets and correlation with generated noise. Journal of Fluid Mechanics 2002; 450: 97–130. DOI:10.1017/s002211200100622x.
7. Settles GS. Schlieren and shadowgraph techniques: visualizing phenomena in transparent media. Springer Science & Business Media, 2001.
8. Fuchs H. Measurement of pressure fluctuations within subsonic turbulent jets. Journal of Sound and Vibration 1972; 22(3): 361–378. DOI:10.1016/0022-460x(72)90171-x.
9. Fuchs H. Space correlations of the fluctuating pressure in subsonic turbulent jets. Journal of Sound and Vibration 1972; 23(1): 77–99. DOI:10.1016/0022-460x(72)90790-0.
10. Mollo-Christensen E. Measurements of near field pressure of subsonic jets. Technical report, Advisory Group for Aeronautical Research and Development Paris, 1963.
11. Jones BG, Adrian RJ, Nithianandan CK et al. Spectra of turbulent static pressure fluctuations in jet mixing layers. AIAA Journal 1979; 17(5): 449–457. DOI:10.2514/3.61154.
12. George WK, Beuther PD and Arndt REA. Pressure spectra in turbulent free shear flows. Journal of Fluid Mechanics 1984; 148: 155–191. DOI:10.1017/s0022112084002299.
13. Jordan P and Colonius T. Wave packets and turbulent jet noise. Annual Review of Fluid Mechanics 2013; 45(1): 173–195. DOI:10.1146/annurev-fluid-011212-140756.

14. Cavalieri AVG, Jordan P and Lesshafft L. Wave-packet models for jet dynamics and sound radiation. Applied Mechanics Reviews 2019; 71(2). DOI:10.1115/1.4042736.
15. Howes WL. Distribution of time-averaged pressure fluctuations along the boundary of a round subsonic jet. NASA Tech Note D-468 1960; .
16. Ribner H. The generation of sound by turbulent jets. In Advances in Applied Mechanics. Elsevier, 1964. pp. 103–182. DOI:10.1016/s0065-2156(08)70354-5.
17. Tinney CE and Jordan P. The near pressure field of co-axial subsonic jets. Journal of Fluid Mechanics 2008; 611: 175–204. DOI:10.1017/s0022112008001833.
18. Cavalieri AVG, Jordan P, Gervais Y et al. Intermittent sound generation and its control in a free-shear flow. Physics of Fluids 2010; 22(11): 115113. DOI:10.1063/1.3517297.
19. Cavalieri AV, Jordan P, Agarwal A et al. Jittering wave-packet models for subsonic jet noise. Journal of Sound and Vibration 2011; 330(18-19): 4474–4492. DOI:10.1016/j.jsv.2011.04.007.
20. Jordan P, Colonius T, Bres G et al. Modeling intermittent wavepackets and their radiated sound in a turbulent jet. In Proceedings of the Summer Program. Center for Turbulence Research, Stanford University, p. 241.
21. Ukeiley LS and Ponton MK. On the near field pressure of a transonic axisymmetric jet. International Journal of Aeroacoustics 2004; 3(1): 43–65. DOI:10.1260/147547204323022257.
22. Grizzi S and Camussi R. Wavelet analysis of near-field pressure fluctuations generated by a subsonic jet. Journal of Fluid Mechanics 2012; 698: 93–124. DOI:10.1017/jfm.2012.64.
23. Mancinelli M, Pagliaroli T, Marco AD et al. Wavelet decomposition of hydrodynamic and acoustic pressures in the near field of the jet. Journal of Fluid Mechanics 2017; 813: 716–749. DOI:10.1017/jfm.2016.869.
24. Kœnig M, Cavalieri AV, Jordan P et al. Farfield filtering and source imaging of subsonic jet noise. Journal of Sound and Vibration 2013; 332(18): 4067–4088. DOI:10.1016/j.jsv.2013.02.040.
25. Mallat S. A wavelet tour of signal processing. Elsevier, 1999.
26. Torrence C and Compo GP. A practical guide to wavelet analysis. Bulletin of the American Meteorological society 1998; 79(1): 61–78.
27. Williams JEF. Hydrodynamic noise. Annual Review of Fluid Mechanics 1969; 1(1): 197–222. DOI: 10.1146/annurev.fl.01.010169.001213.
28. Petitjean BP, Viswanathan K and McLaughlin DK. Acoustic pressure waveforms measured in high speed jet noise experiencing nonlinear propagation. International Journal of Aeroacoustics 2006; 5(2): 193–215. DOI: 10.1260/147547206777629835.
29. Donoho DL and Johnstone IM. Ideal spatial adaptation by wavelet shrinkage. Biometrika 1994; 81(3): 425–455. DOI:10.1093/biomet/81.3.425.
30. Rackl R and Siddon TE. Causality correlation analysis of flow noise with fluid dilatation as source fluctuation. The Journal of the Acoustical Society of America 1979; 65(5): 1147–1155. DOI:10.1121/1.382781.
31. Bogey C and Bailly C. An analysis of the correlations between the turbulent flow and the sound pressure fields of subsonic jets. Journal of Fluid Mechanics 2007; 583: 71–97. DOI:10.1017/s002211200700612x.
32. Jordan P and Gervais Y. Subsonic jet aeroacoustics: associating experiment, modelling and simulation. Experiments in Fluids 2007; 44(1): 1–21. DOI:10.1007/s00348-007-0395-y.
33. Lee H, Uzun A and Hussaini MY. Identification of jet noise source using causality method based on large-eddy simulation of a round jet flow. International Journal of Aeroacoustics 2016; 16(1-2): 78–96. DOI: 10.1177/1475472x16680465.
34. Mathew J, Bahr C, Carroll B et al. Design, fabrication, and characterization of an anechoic wind tunnel facility. In 11th AIAA/CEAS Aeroacoustics Conference. 2005-3052. DOI:10.2514/6.2005-3052.

35. Li S, Ukeiley LS and Sheplak M. PIV measurements and reduced-order characterization of a mach 0.3 axisymmetric jet. In AIAA Scitech 2020 Forum. 2020-2039. DOI:10.2514/6.2020-2039.
36. Soderman PT and Allen CS. Microphone measurements in and out of airstream. In Aeroacoustic Measurements. Springer Berlin Heidelberg, 2002. pp. 1–61. DOI:10.1007/978-3-662-05058-3_1.
37. Taniguchi H and Rasmussen G. Selection and use of microphones for engine and aircraft noise measurements. Brüel and Kjaer Technical Review No 4 (reprint from Sound and Vibration, Feb 1979) 1979; .
38. Sreenivasan KR, Antonia RA and Britz D. Local isotropy and large structures in a heated turbulent jet. Journal of Fluid Mechanics 1979; 94(4): 745–775. DOI:10.1017/s0022112079001270.
39. Glauser MN and George WK. Orthogonal decomposition of the axisymmetric jet mixing layer including azimuthal dependence. In Advances in Turbulence. Springer Berlin Heidelberg, 1987. pp. 357–366. DOI: 10.1007/978-3-642-83045-7_40.
40. Iqbal MO and Thomas FO. Coherent structure in a turbulent jet via a vector implementation of the proper orthogonal decomposition. Journal of Fluid Mechanics 2007; 571: 281–326. DOI:10.1017/ s0022112006003351.
41. Gamard S, Jung D and George WK. Downstream evolution of the most energetic modes in a turbulent axisymmetric jet at high reynolds number. part 2. the far-field region. Journal of Fluid Mechanics 2004; 514: 205–230. DOI:10.1017/s0022112004000175.
42. Tinney CE, Glauser MN and Ukeiley LS. Low-dimensional characteristics of a transonic jet. part 1. proper orthogonal decomposition. Journal of Fluid Mechanics 2008; 612: 107–141. DOI:10.1017/ s0022112008002978.
43. Bodony D. The prediction and understanding of jet noise. Center for Turbulence Research Annual Research Briefs 2005; : 367 – 377.
44. Tanna H. An experimental study of jet noise part i: Turbulent mixing noise. Journal of Sound and Vibration 1977; 50(3): 405–428. DOI:10.1016/0022-460x(77)90493-x.
45. Brown C and Bridges J. Small hot jet acoustic rig validation. NASA/TM-2006-214234, E-15481 2006; .
46. Cavalieri AVG, Jordan P, Colonius T et al. Axisymmetric superdirectivity in subsonic jets. Journal of Fluid Mechanics 2012; 704: 388–420. DOI:10.1017/jfm.2012.247.
47. Tam CKW, Viswanathan K, Ahuja KK et al. The sources of jet noise: experimental evidence. Journal of Fluid Mechanics 2008; 615: 253–292. DOI:10.1017/s0022112008003704.
48. Sim B and Hall J. Streamwise variation of the unsteady pressure field in the three-dimensional wall jet. In AIAA Scitech 2020 Forum. 2020-2037. DOI:10.2514/6.2020-2037.
49. Bendat JS and Piersol AG. Random data: analysis and measurement procedures, volume 729. John Wiley & Sons, 2011.
50. Arndt REA, Long DF and Glauser MN. The proper orthogonal decomposition of pressure fluctuations surrounding a turbulent jet. Journal of Fluid Mechanics 1997; 340: 1–33. DOI:10.1017/s0022112097005089.
51. Ponton MK, Ukeiley LS and Lee SW. Aeroacoustic data for a high reynolds number axisymmetric subsonic jet. NASA/TM-1999-209336, L-17870 1999; .
52. Lau J, Fisher M and Fuchs H. The intrinsic structure of turbulent jets. Journal of Sound and Vibration 1972; 22(4): 379–406. DOI:10.1016/0022-460x(72)90451-8.
53. Cavalieri AVG, Rodríguez D, Jordan P et al. Wavepackets in the velocity field of turbulent jets. Journal of Fluid Mechanics 2013; 730: 559–592. DOI:10.1017/jfm.2013.346.
54. Batchelor GK and Gill AE. Analysis of the stability of axisymmetric jets. Journal of Fluid Mechanics 1962; 14(04): 529. DOI:10.1017/s0022112062001421.